# Science Advances

**MAAAS**

## Supplementary Materials for

## Lighting up metastasis process before formation of secondary tumor by phosphorescence imaging

Kai Chang *et al.*

Corresponding author: Yufeng Zhang, zyf@whu.edu.cn; Qianqian Li, liqianqian@whu.edu.cn; Zhen Li, lizhen@whu.edu.cn

**This PDF file includes:**

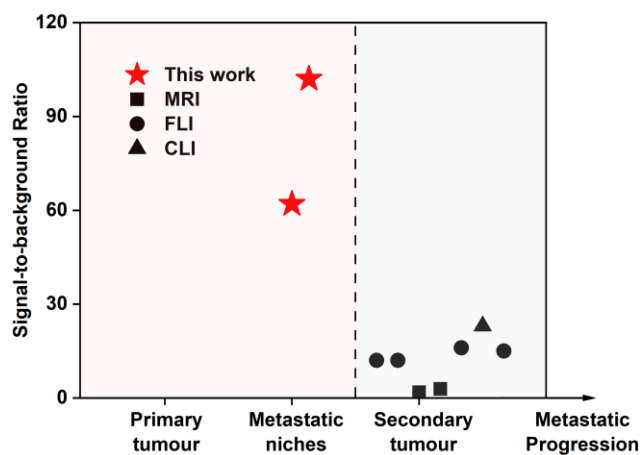Figs. S1 to S23
Tables S1 and S2
References

**Fig. S1.** Signal-to-Background Ratio (SBR) and corresponding metastatic stages of current technologies reported in literatures and our work.
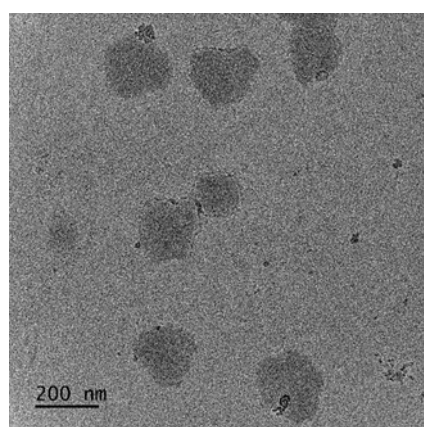


**Fig. S2.** Representative transmission electron microscopy (TEM) images of prepared NPs.
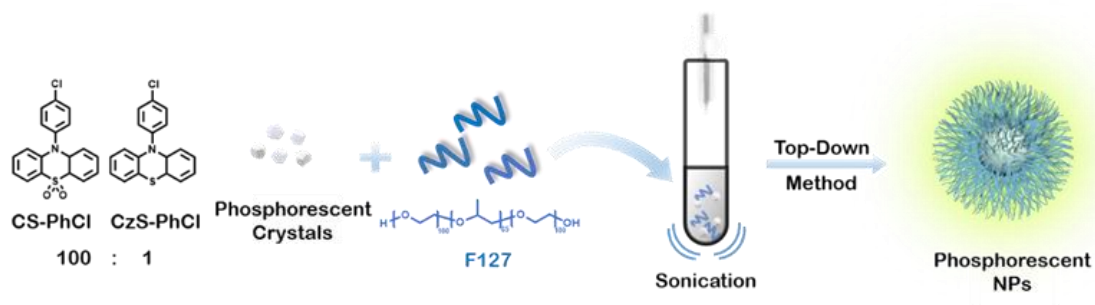


**Fig. S3.** Schematic diagram of fabrication processes of phosphorescence NPs.
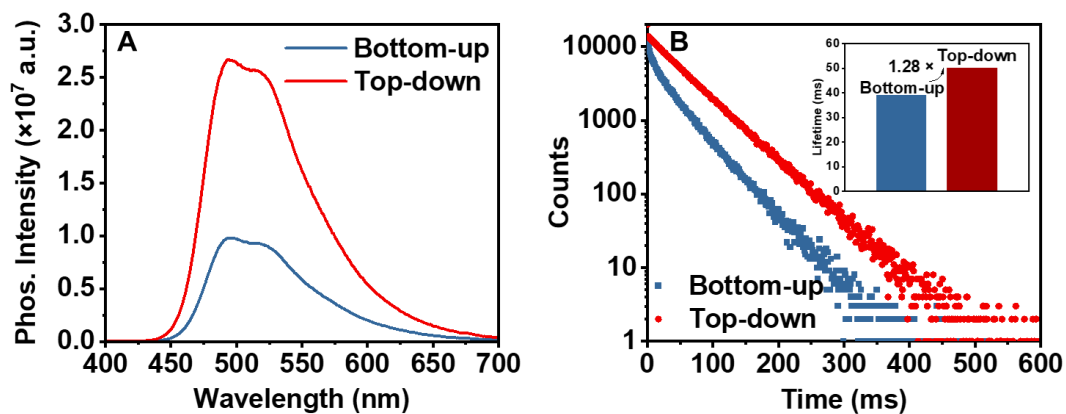
**Fig. S4.** The RTP property of NPs by bottom-up and top-down methods. (A) Phosphorescence spectra of nanoparticles, (B) Phosphorescence delay of nanoparticles.
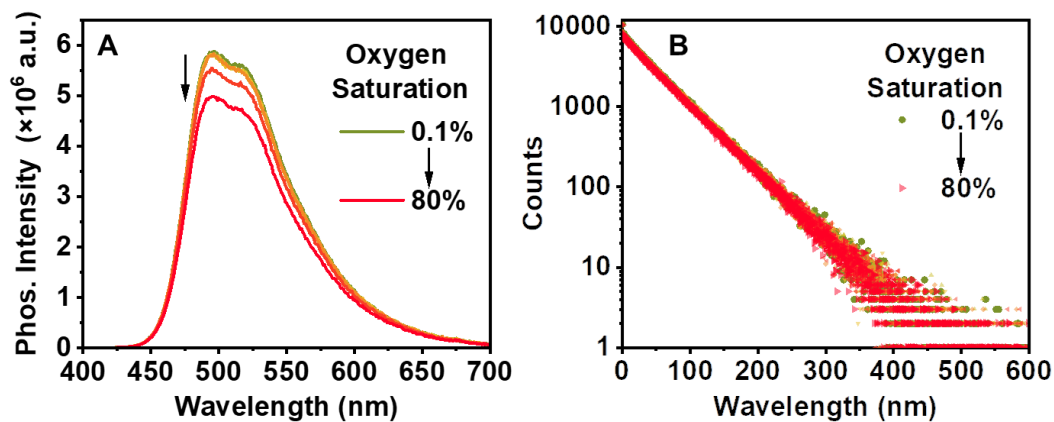


**Fig. S5.** The RTP property of NPs with different oxygen saturation in PBS solution. The phosphorescence spectra (A) and the phosphorescence decay (B) of NPs with the oxygen saturation ranging from 0.1% to 80%.
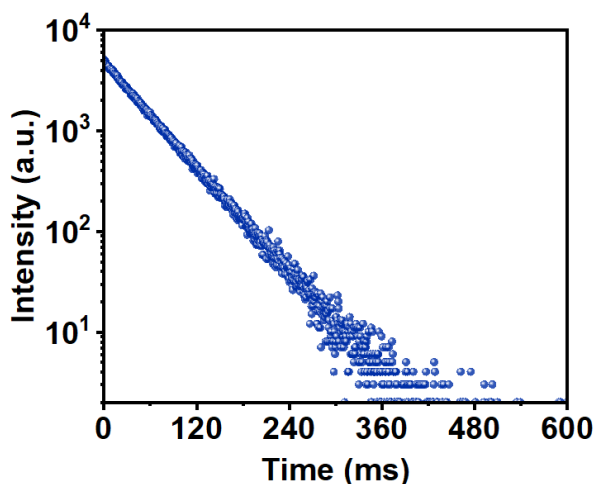
**Fig. S6.** RTP decay curves of NPs determined by FLS980.
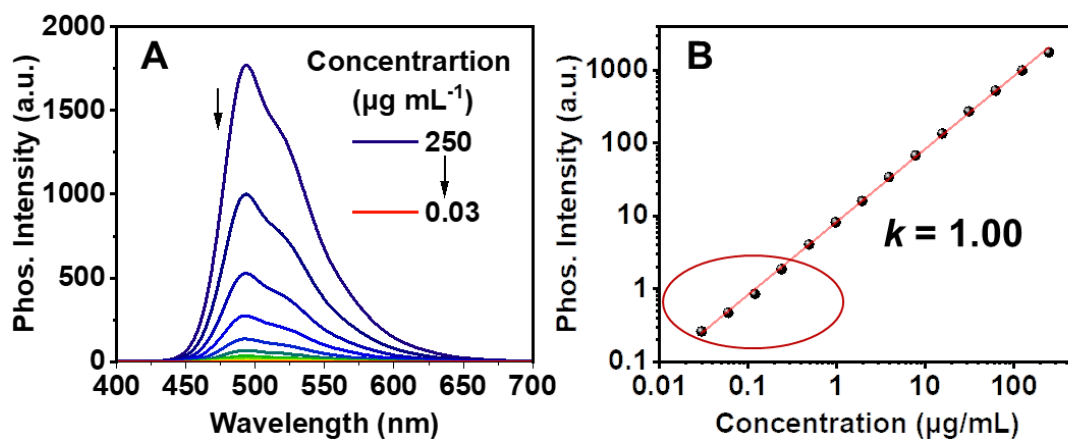


**Fig. S7.** Comparison of fluorescence and phosphorescence sensitivity by fluoresceine and phosphorescence NPs. The phosphorescence intensity (A) and the maximum emission intensity (B) of phosphorescence NPs with concentration ranging from 250 µg mL$^{-1}$ to 0.03 µg mL$^{-1}$.
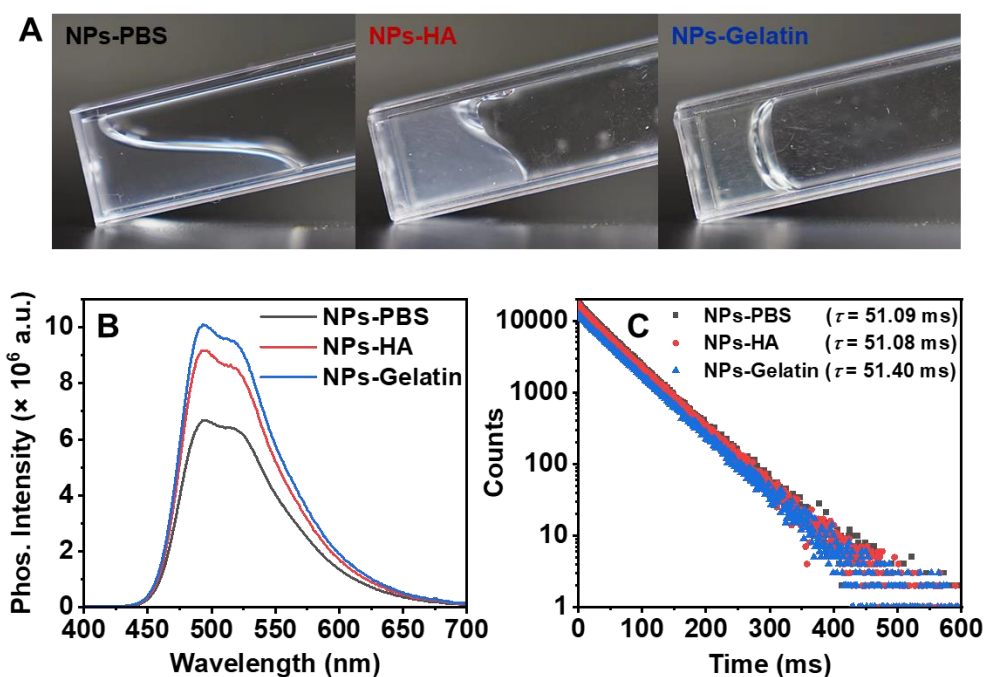
**Fig. S8.** Stiffness response of phosphorescence NPs under different environment. The photographs (A), phosphorescence spectra (B) and lifetimes (C) of phosphorescence NPs in PBS, 10% HA, and 15% gelatin solutions.
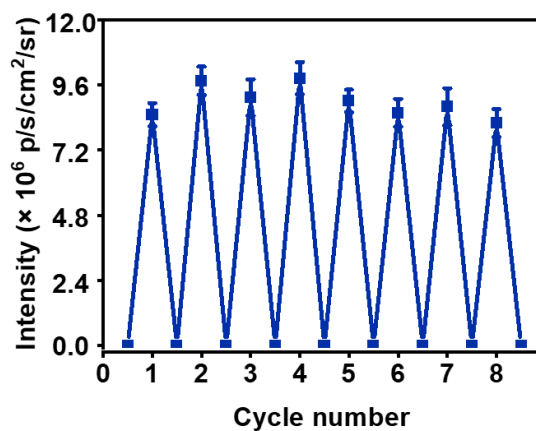


**Fig. S9.** The phosphorescence intensities of NPs as a function of the cycle number of light activations. (n = 3, mean ± s.d.).
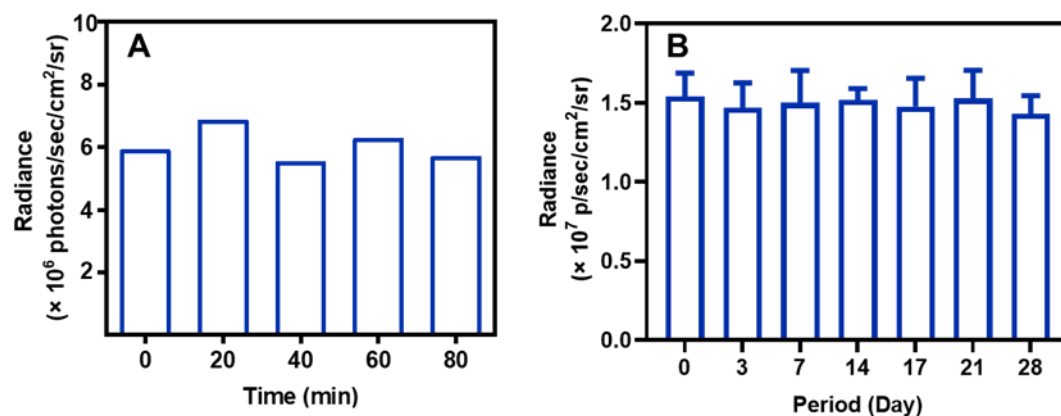
**Fig. S10.** (A) The afterglow intensities of NPs with varied UV exposure time. (B) The afterglow intensities of NPs after storage for different days at 4 °C (n = 3, mean ± s.d.).
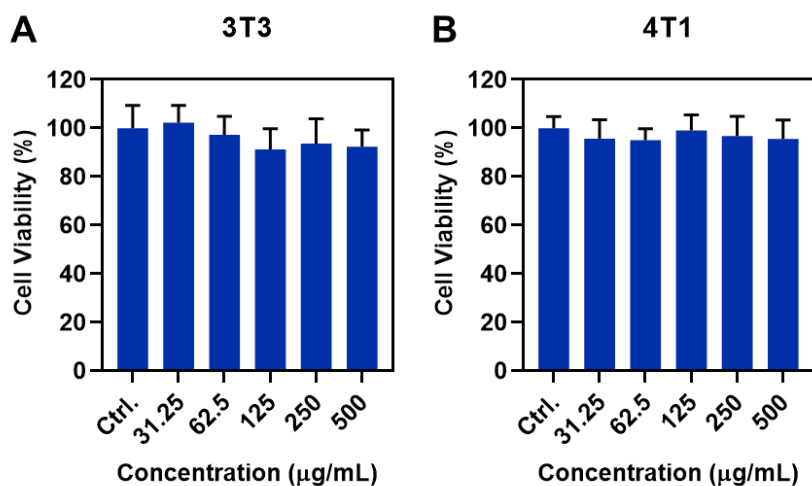


**Fig. S11.** Cell viabilities of NIH/3T3 (A) and 4T1 (B) cells after incubation with NPs in different concentration. (n = 3, mean ± s.d.).
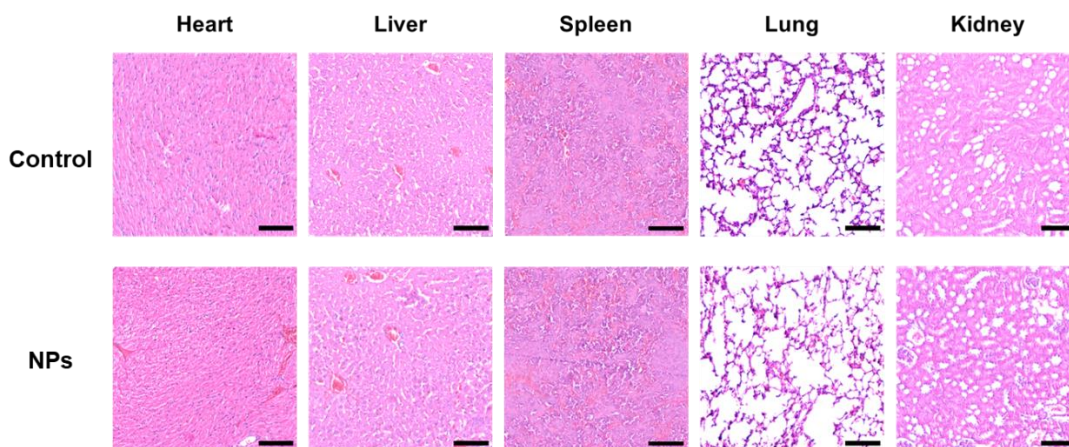
**Fig. S12.** H&E-stained images of major organs of the normal mice after intravenous injection of PBS (control) and NPs (n = 3). The scale bars represent 100 μm.
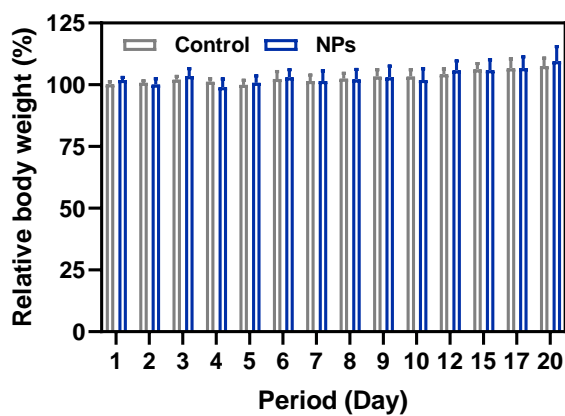


**Fig. S13.** Changes of relative body weight of healthy BALB/c mice after intravenous injection of PBS and NPs from day 1 to day 20 (n = 3, mean ± s.d.).
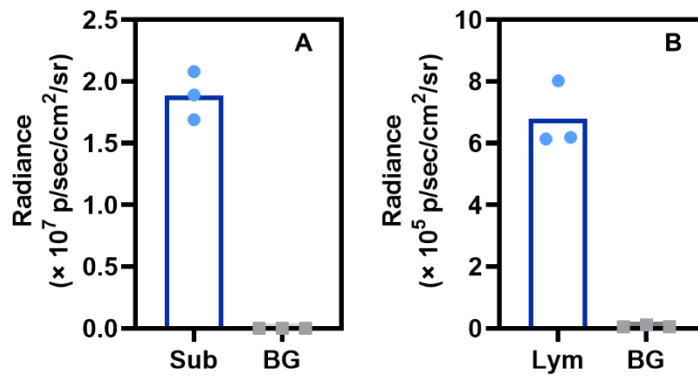
**Fig. S14.** Signal and background radiance of pre-irradiated subcutaneous imaging (A) and lymph node imaging (B) (n = 3).
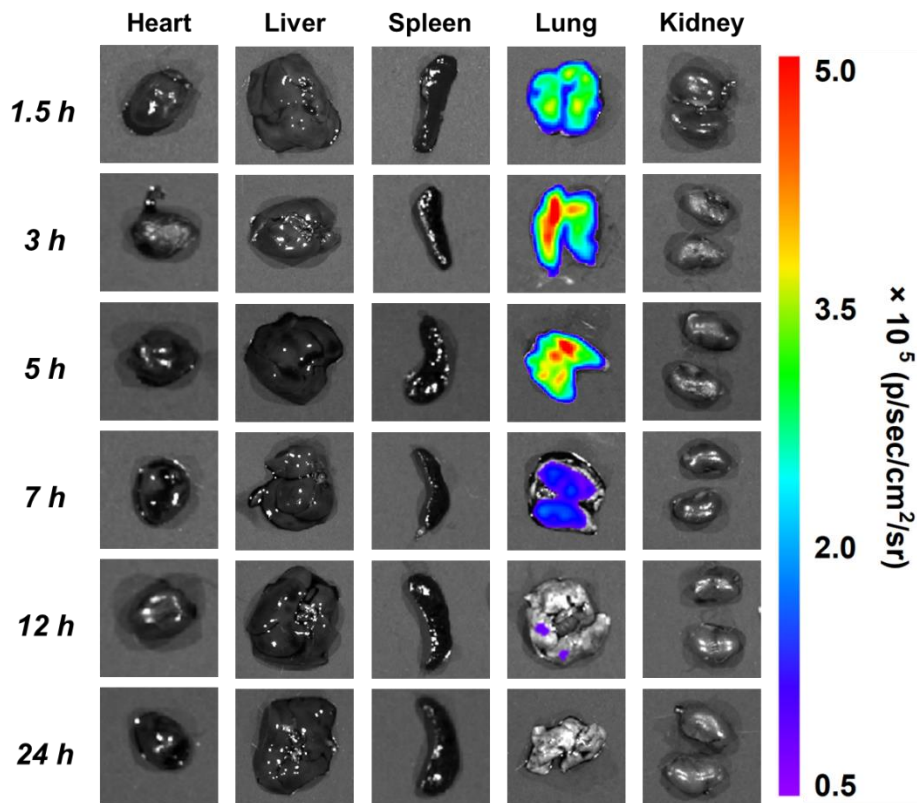


**Fig. S15.** Phosphorescence imaging of isolated organs (hearts, livers, spleens, lungs and kidneys) from mice bearing 4T1 metastatic tumors at 1.5 h, 3 h, 5 h, 7 h, 12 h and 24 h post intravenous injection of NPs after removal of light irradiation at t = 10 s.
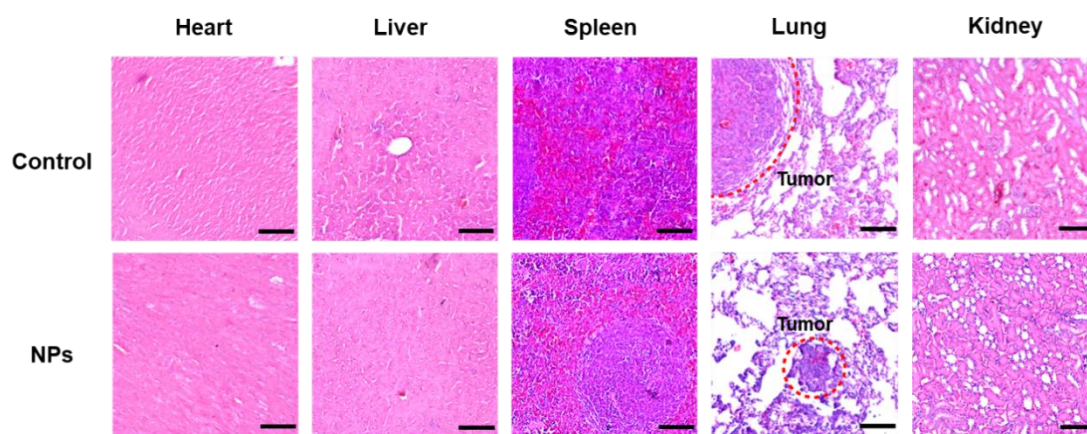
**Fig. S16.** H&E-stained images of major organs of the mice bearing 4T1 lung metastases after intravenous injection of NPs. The scale bars represent 100 μm.
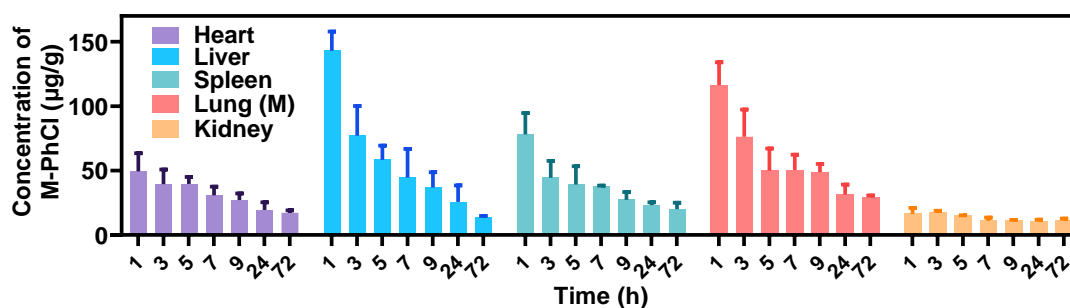


**Fig. S17.** NPs concentration in different organs from mice bearing 4T1 metastatic tumors at 1.5 h, 3 h, 5 h, 7 h, 12 h and 24 h post intravenous injection. (M, metastases) (n = 3, mean ± s.d.).
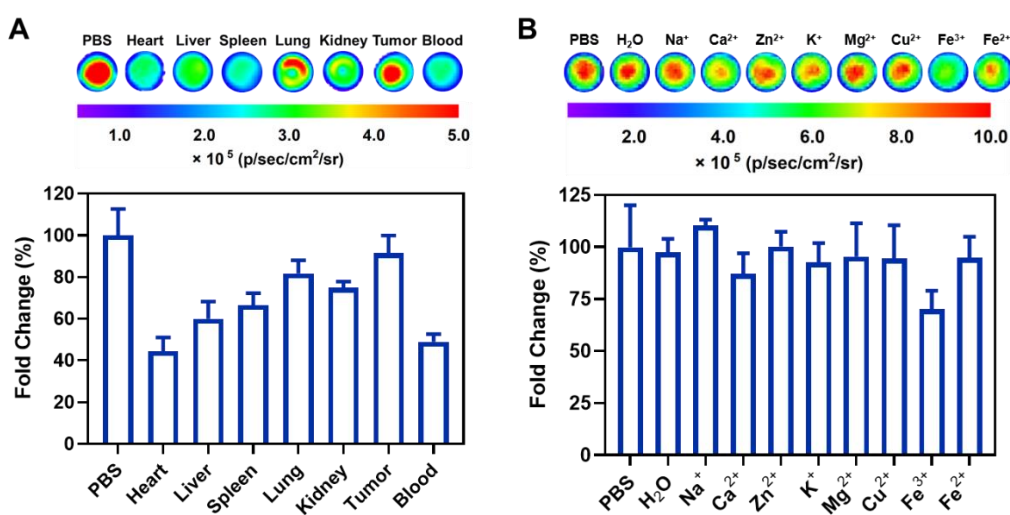


**Fig. S18.** Phosphorescence images captured by IVIS spectrum and plot of fold changes of phosphorescence intensities for NPs after incubation with different tissue homogenates (A) and different metal ions (B), respectively (n = 3, mean ± s.d.)
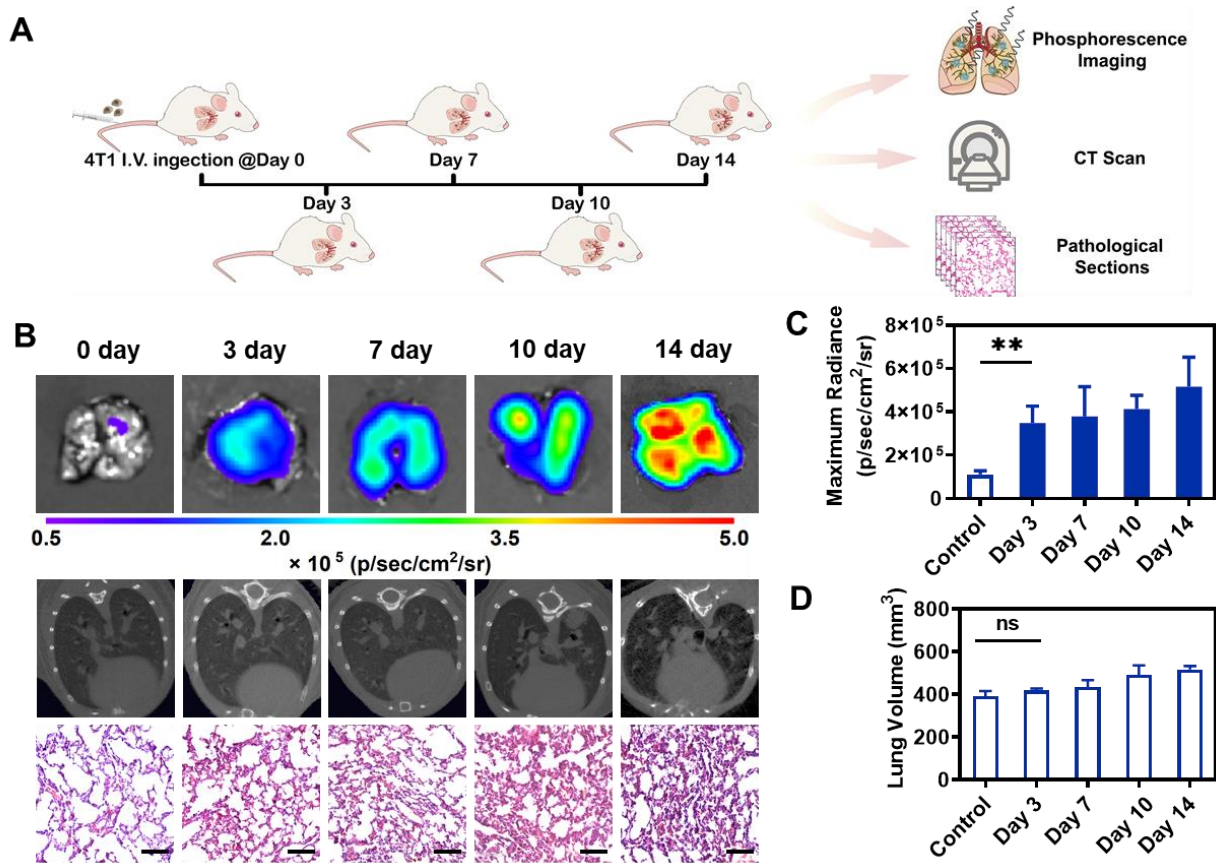
**Fig. S19.** (A) Schematic diagram of 4T1 lung metastatic tumor and lungs monitored by phosphorescence imaging, CT scan and pathological sections. (B) Phosphorescence images, CT images, and H&E-stained images of 4T1 metastatic lungs from day 0 to day 14 (n = 3). Scale bar: 100 μm. (C) Maximum radiance of phosphorescence imaging of 4T1 metastatic lungs from day 0 to day 14 (n = 3, mean ± s.d.). (D) Lung volume of 4T1 metastatic lungs from day 0 to day 14 calculated by Analyze 14.0 software (n = 3, mean ± s.d.).
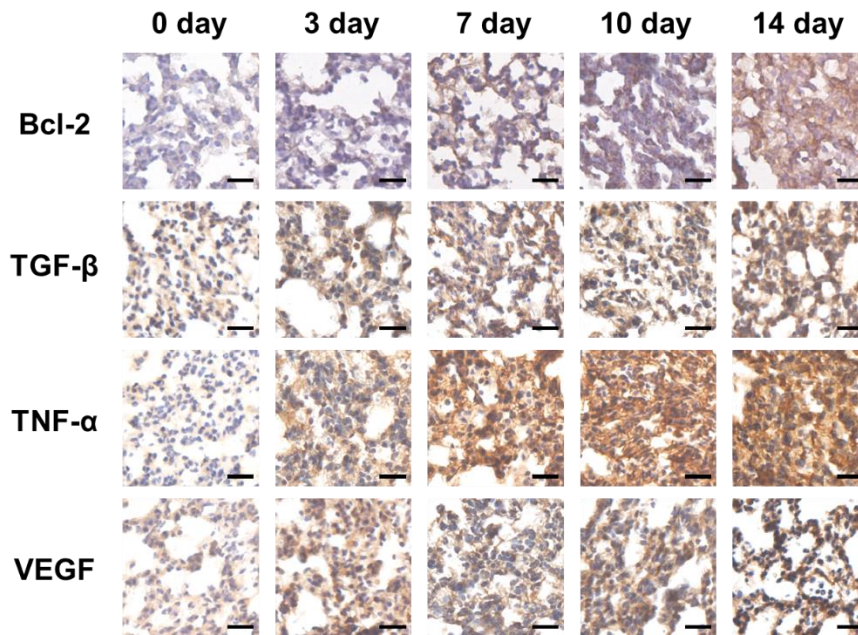
**Fig. S20.** IHC staining of Bcl-2, TGF-β, TNF-α and VEGF of 4T1 metastatic lungs from day 0 to day 14 (n = 3). Scale bar: 20 μm.
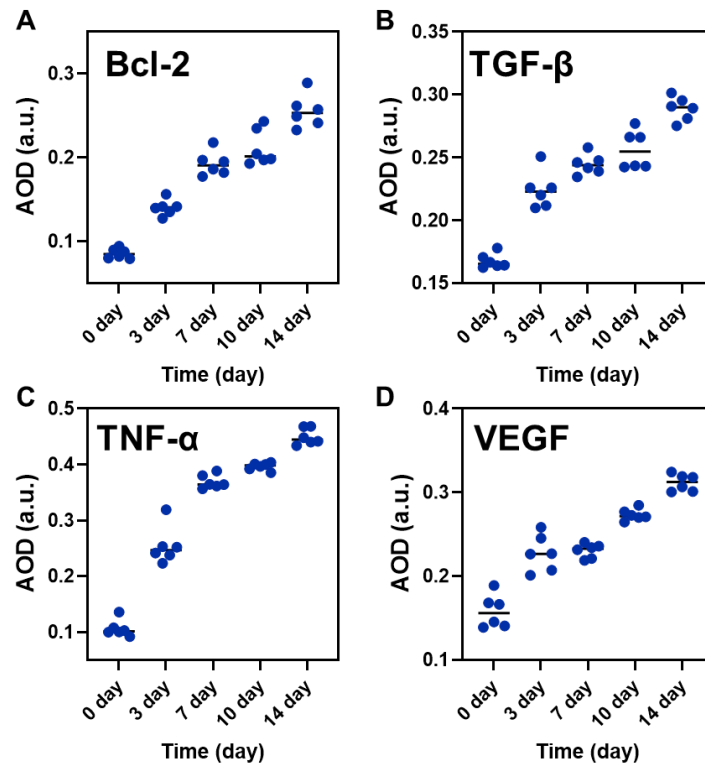


**Fig. S21.** Average optical density (AOD) of corresponding IHC stained images calculated by ImageJ software. A: Bcl-2. B: TGF-β. C: TNF-α. D: VEGF (n = 6).
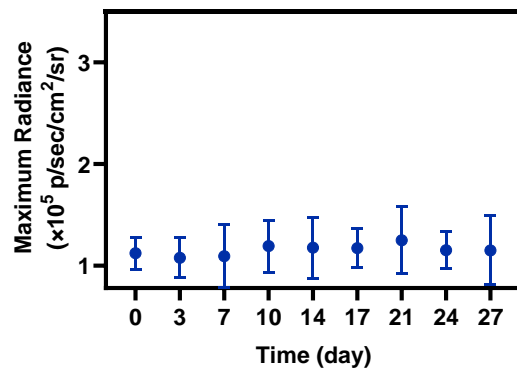
**Fig. S22.** Maximum radiance of lungs of control mice from day 0 to day 27 (n = 3, mean ± s.d.).
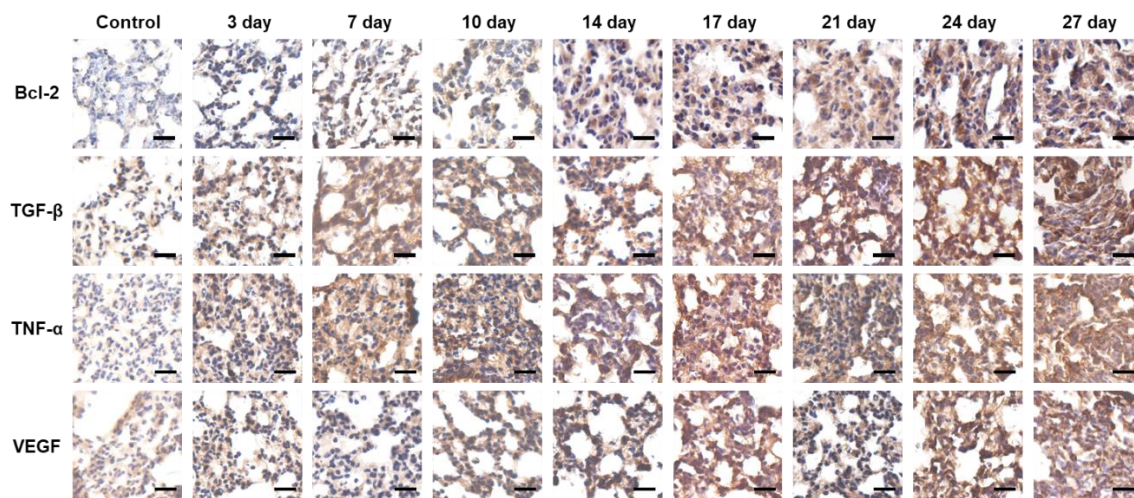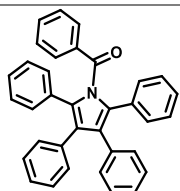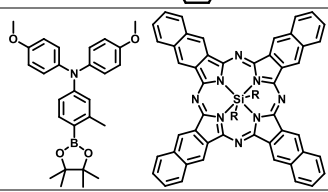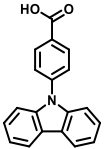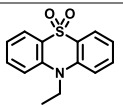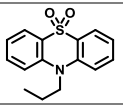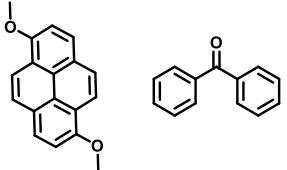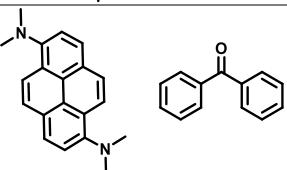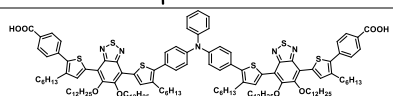


**Fig. S23.** IHC staining of Bcl-2, TGF-β, TNF-α and VEGF of orthotopic H22 liver tumor metastatic lungs from day 0 to day 27 (n = 3). Scale bar: 20 μm.

| Technologies | Metastatic target organ | Metastatic pathway | Orthotopic metastatic models | Diagnosed metastatic stage | SBR | Reference |
|---|---|---|---|---|---|---|
| **Phosphorescence imaging** | Lung | Blood-stream | No | Pre-metastatic microenvironmental changes | 102 | **This work** |
| **Phosphorescence imaging** | Lung | Blood-stream | Yes | Pre-metastatic microenvironmental changes | 62 | **This work** |
| **Fluorescence imaging** | Lung Liver Pancreas Kidney Bone | Blood-stream | No | Secondary tumor | 12 | (*11*) |
| **Fluorescence imaging** | Peritoneum | / | Yes | Secondary tumor | 12 | (*12*) |
| **Fluorescence imaging** | Back | / | No | Secondary tumor | 16 | (*13*) |
| **Fluorescence imaging & Naked eye** | Lymph node | Lymphatic system | No | Secondary tumor | / | (*50*) |
| **Optoacoustic imaging** | Lymph node | Lymphatic system | No | Secondary tumor | / | (*51*) |
| **MRI** | Liver | / | No | Secondary tumor | 1.8 | (*15*) |
| **MRI** | Liver | Blood-stream | No | Secondary tumor | 2.9 | (*52*) |
| **MRI & PET** | Lymph node | Lymphatic system | No | Secondary tumor | / | (*53*) |
| **PET & Urine test** | Lung | Blood-stream | No | Secondary tumor | / | (*16*) |

| | | | | | | |
|---|---|---|---|---|---|---|
| **Micro-CT & FMT & MRI** | Liver Lung | Blood-stream | Yes | Secondary tumor | 15 | (*17*) |
| **Chemiluminescence imaging** | Peritoneum | / | No | Secondary tumor | 23 | (*20*) |

**Table S1. Comparison of NPs with other imaging methods in terms of metastatic site, metastatic pathway, diagnosed metastatic stages and signal to background ratio.**

| Sample | Molecular structure | Quantum yield | Phos. lifetime | Subcutaneous signal to noise ratio (SBR) | Reference |
|---|---|---|---|---|---|
| **TPM (No.1)** |  | 3.7 % | 20.1 μs | 7 | (*54*) |
| **m-TPA-N (No.2)** |  | 17 % (11 %) * | 0.025 s (9.3 μs) * | 51 | (*35*) |
| **4-BACZ (No.3)** |  | 53 % | 0.55 s | 62 | (*55*) |
| **CS-C$_2$H$_5$ (No.4)** |  | 3.5 % | 0.092 s | 30 | (*56*) |
| **CS-C$_3$H$_7$ (No.5)** |  | 5.7 % | 0.327 s | 70 | |
| **DMOPy/BPO (No.6)** |  | 18 % | 0.11 s | 75 | (*27*) |
| **DMAPy/BPO (No.7)** |  | 20 % | 0.18 s | 160 | |
| **d-DTBT (No.8)** |  | 20 % | 0.28 s | 4 | (*26*) |

| Compound | Structure | QY | Lifetime | SBR | Ref |
|---|---|---|---|---|---|
| **t-DTBT** (No.9) |  | 11 % | 0.30 s | 17 | |
| **s-DTBT** (No.10) |  | 32 % | 0.34 s | 230 | |
| **M-C$_2$H$_5$** (No.11) |  | 43 % | 33 s | 147 | *(25)* |
| **M-CH$_3$** (No.12) |  | 20 % | 17 s | 310 | |
| **CBA-CH$_3$** (No.13) |  | 52 % | 0.868 s | 367 | *(39)* |
| **XCO-PiCl** (No.14) |  | 5.4 % | 0.61 s | 375 | *(57)* |
| **m-PBCM** (No.15) |  | 13 % | 0.71 s | 428 | *(58)* |
| **OSN1-T** (No.16) |  | 4.9 % (11 %) * | 0.861 | 444 | *(31)* |
| **M-PhCl** (No.17) |  | 55 % (23 %) * | 6.38 s (49 ms) * | 2278 | **This work** |
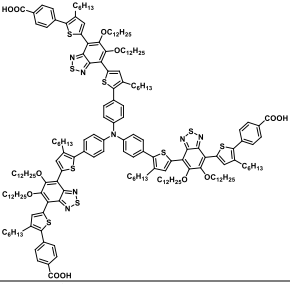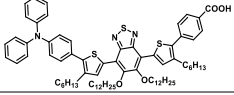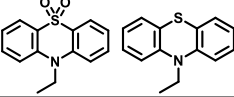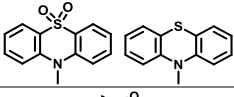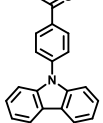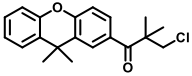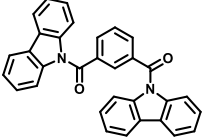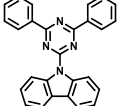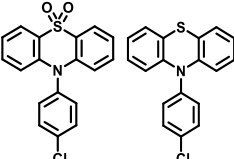
**Table S2. Signal-to-background ratio (SBR) of subcutaneous imaging and corresponding lifetimes of pure organic RTP materials reported in literatures and our work.** (*Quantum yield or phosphorescence lifetime of prepared nanoparticles)

**REFERENCES AND NOTES**

1. R. L. Siegel, K. D. Miller, H. E. Fuchs, A. Jemal, Cancer statistics, 2021. *CA Cancer J. Clin.* **71**, 7–33 (2021).

2. S. Valastyan, R. A. Weinberg, Tumor metastasis: Molecular insights and evolving paradigms. *Cell* **147**, 275–292 (2011).

3. J. Massague, A. C. Obenauf, Metastatic colonization by circulating tumour cells. *Nature* **529**, 298–306 (2016).

4. W. Yu, C. Hu, H. Gao, Advances of nanomedicines in breast cancer metastasis treatment targeting different metastatic stages. *Adv. Drug Deliv. Rev.* **178**, 113909 (2021).

5. P. S. Steeg, Targeting metastasis. *Nat. Rev. Cancer* **16**, 201–218 (2016).

6. Y. Liu, X. Cao, Characteristics and significance of the pre-metastatic niche. *Cancer Cell* **30**, 668–681 (2016).

7. D. F. Quail, J. A. Joyce, Microenvironmental regulation of tumor progression and metastasis. *Nat. Med.* **19**, 1423–1437 (2013).

8. A. Schroeder, D. A. Heller, M. M. Winslow, J. E. Dahlman, G. W. Pratt, R. Langer, T. Jacks, D. G. Anderson, Treating metastatic cancer with nanotechnology. *Nat. Rev. Cancer* **12**, 39–50 (2011).

9. N. K. Altorki, G. J. Markowitz, D. Gao, J. L. Port, A. Saxena, B. Stiles, T. McGraw, V. Mittal, The lung microenvironment: An important regulator of tumour growth and metastasis. *Nat. Rev. Cancer* **19**, 9–31 (2019).

10. S. P. Rowe, M. G. Pomper, Molecular imaging in oncology: Current impact and future directions. *CA Cancer J. Clin.* **72**, 333–352 (2022).

11. H. Xiong, H. Zuo, Y. Yan, G. Occhialini, K. Zhou, Y. Wan, D. J. Siegwart, High-contrast fluorescence detection of metastatic breast cancer including bone and liver micrometastases via size-controlled pH-activatable water-soluble probes. *Adv. Mater.* **29**, 1700131 (2017).

12. P. Wang, Y. Fan, L. Lu, L. Liu, L. Fan, M. Zhao, Y. Xie, C. Xu, F. Zhang, NIR-II nanoprobes in-vivo assembly to improve image-guided surgery for metastatic ovarian cancer. *Nat. Commun.* **9**, 2898 (2018).

13. Y. Li, S. Zeng, J. Hao, Non-invasive optical guided tumor metastasis/vessel imaging by using lanthanide nanoprobe with enhanced down-shifting emission beyond 1500 nm. *ACS Nano* **13**, 248–259 (2019).

14. H. Cao, L. Zou, B. He, L. Zeng, Y. Huang, H. Yu, P. Zhang, Q. Yin, Z. Zhang, Y. Li, Albumin biomimetic nanocorona improves tumor targeting and penetration for synergistic therapy of metastatic breast cancer. *Adv. Funct. Mater.* **27**, 1605679 (2017).

15. P. Mi, D. Kokuryo, H. Cabral, H. Wu, Y. Terada, T. Saga, I. Aoki, N. Nishiyama, K. Kataoka, A pH-activatable nanoparticle with signal-amplification capabilities for non-invasive imaging of tumour malignancy. *Nat. Nanotechnol.* **11**, 724–730 (2016).

16. L. Hao, N. Rohani, R. T. Zhao, E. M. Pulver, H. Mak, O. J. Kelada, H. Ko, H. E. Fleming, F. B. Gertler, S. N. Bhatia, Microenvironment-triggered multimodal precision diagnostics. *Nat. Mater.* **20**, 1440–1448 (2021).

17. P. M. Peiris, R. Toy, E. Doolittle, J. Pansky, A. Abramowski, M. Tam, P. Vicente, E. Tran, E. Hayden, A. Camann, A. Mayer, B. O. Erokwu, Z. Berman, D. Wilson, H. Baskaran, C. A. Flask, R. A. Keri, E. Karathanasis, Imaging metastasis using an integrin-targeting chain-shaped nanoparticle. *ACS Nano* **6**, 8783–8795 (2012).

18. H. Peinado, H. Zhang, I. R. Matei, B. Costa-Silva, A. Hoshino, G. Rodrigues, B. Psaila, R. N. Kaplan, J. F. Bromberg, Y. Kang, M. J. Bissell, T. R. Cox, A. J. Giaccia, J. T. Erler, S. Hiratsuka, C. M. Ghajar, D. Lyden, Pre-metastatic niches: Organ-specific homes for metastases. *Nat. Rev. Cancer* **17**, 302–317 (2017).

19. M. Keyaerts, V. Caveliers, T. Lahoutte, Bioluminescence imaging: Looking beyond the light. *Trends Mol. Med.* **18**, 164–172 (2012).

20. W. Chen, Y. Zhang, Q. Li, Y. Jiang, H. Zhou, Y. Liu, Q. Miao, M. Gao, Near-infrared afterglow luminescence of chlorin nanoparticles for ultrasensitive in vivo imaging. *J. Am. Chem. Soc.* **144**, 6719–6726 (2022).

21. J. Huang, K. Pu, Activatable molecular probes for second near-infrared fluorescence, chemiluminescence, and photoacoustic imaging. *Angew. Chem. Int. Edit.* **59**, 11717–11731 (2020).

22. W. Zhao, Z. He, B. Z. Tang, Room-temperature phosphorescence from organic aggregates. *Nat. Rev. Mater.* **5**, 869–885 (2020).

23. M. Fang, J. Yang, Z. Li, Light emission of organic luminogens: Generation, mechanism and application. *Prog. Mater. Sci.* **125**, 100914 (2022).

24. A. Huang, Q. Li, Z. Li, Molecular uniting set identified characteristic (MUSIC) of organic optoelectronic material. *Chin. J. Chem.* **40**, 2356–2370 (2022).

25. Y. Wang, H. Gao, J. Yang, M. Fang, D. Ding, B. Z. Tang, Z. Li, High performance of simple organic phosphorescence host–guest materials and their application in time-resolved bioimaging. *Adv. Mater.* **33**, 2007811 (2021).

26. Y. Fan, S. Liu, M. Wu, L. Xiao, Y. Fan, M. Han, K. Chang, Y. Zhang, X. Zhen, Q. Li, Z. Li, Mobile phone flashlight-excited red afterglow bioimaging. *Adv. Mater.* **34**, 2201280 (2022).

27. F. Xiao, H. Gao, Y. Lei, W. Dai, M. Liu, X. Zheng, Z. Cai, X. Huang, H. Wu, D. Ding, Guest-host doped strategy for constructing ultralong-lifetime near-infrared organic phosphorescence materials for bioimaging. *Nat. Commun.* **13**, 186 (2022).

28. L. Wan, K. Pantel, Y. Kang, Tumor metastasis: Moving new biological insights into the clinic. *Nat. Med.* **19**, 1450–1464 (2013).

29. A. W. Lambert, D. R. Pattabiraman, R. A. Weinberg, Emerging biological principles of metastasis. *Cell* **168**, 670–691 (2017).

30. A. R. Delbridge, S. Grabow, A. Strasser, D. L. Vaux, Thirty years of BCL-2: Translating cell death discoveries into novel cancer therapies. *Nat. Rev. Cancer* **16**, 99–109 (2016).

31. X. Zhen, Y. Tao, Z. An, P. Chen, C. Xu, R. Chen, W. Huang, K. Pu, Ultralong phosphorescence of water-soluble organic nanoparticles for in vivo afterglow imaging. *Adv. Mater.* **29**, 1606665 (2017).

32. Y. Wang, J. Yang, M. Fang, Y. Gong, J. Ren, L. Tu, B. Z. Tang, Z. Li, New phenothiazine derivatives that exhibit photoinduced room-temperature phosphorescence. *Adv. Funct. Mater.* **31**, 2101719 (2021).

33. Q. Li, Z. Li, Molecular packing: Another key point for the performance of organic and polymeric optoelectronic materials. *Acc. Chem. Res.* **53**, 962–973 (2020).

34. X. Wu, Y. Jiang, N. J. Rommelfanger, F. Yang, Q. Zhou, R. Yin, J. Liu, S. Cai, W. Ren, A. Shin, K. S. Ong, K. Pu, G. Hong, Tether-free photothermal deep-brain stimulation in freely behaving mice via wide-field illumination in the near-infrared-II window. *Nat. Biomed. Eng.* **6**, 754–770 (2022).

35. Q. Dang, Y. Jiang, J. Wang, J. Wang, Q. Zhang, M. Zhang, S. Luo, Y. Xie, K. Pu, Q. Li, Z. Li, Room-temperature phosphorescence resonance energy transfer for construction of near-infrared afterglow imaging agents. *Adv. Mater.* **32**, 2006752 (2020).

36. C. Zhang, Z. Zeng, D. Cui, S. He, Y. Jiang, J. Li, J. Huang, K. Pu, Semiconducting polymer nano-PROTACs for activatable photo-immunometabolic cancer therapy. *Nat. Commun.* **12**, 2934 (2021).

37. Z. Cong, M. Han, Y. Fan, Y. Fan, K. Chang, L. Xiao, Y. Zhang, X. Zhen, Q. Li, Z. Li, Ultralong blue room-temperature phosphorescence by cycloalkyl engineering. *Mater. Chem. Front.* **6**, 1606–1614 (2022).

38. J. Yang, X. Zhen, B. Wang, X. Gao, Z. Ren, J. Wang, Y. Xie, J. Li, Q. Peng, K. Pu, Z. Li, The influence of the molecular packing on the room temperature phosphorescence of purely organic luminogens. *Nat. Commun.* **9**, 840 (2018).

39. H. Gao, Z. Gao, D. Jiao, J. Zhang, X. Li, Q. Tang, Y. Shi, D. Ding, Boosting room temperature phosphorescence performance by alkyl modification for intravital orthotopic lung tumor imaging. *Small* **17**, 2005449 (2021).

40. N. Bertrand, P. Grenier, M. Mahmoudi, E. M. Lima, E. A. Appel, F. Dormont, J.-M. Lim, R. Karnik, R. Langer, O. C. Farokhzad, Mechanistic understanding of in vivo protein corona formation on polymeric nanoparticles and impact on pharmacokinetics. *Nat. Commun.* **8**, 777 (2017).

41. G. Francia, W. Cruz-Munoz, S. Man, P. Xu, R. S. Kerbel, Mouse models of advanced spontaneous metastasis for experimental therapeutics. *Nat. Rev. Cancer* **11**, 135–141 (2011).

42. C. Liang, L. Xu, G. Song, Z. Liu, Emerging nanomedicine approaches fighting tumor metastasis: Animal models, metastasis-targeted drug delivery, phototherapy, and immunotherapy. *Chem. Soc. Rev.* **45**, 6250–6269 (2016).

43. B. A. Aguado, G. G. Bushnell, S. S. Rao, J. S. Jeruss, L. D. Shea, Engineering the pre-metastatic niche. *Nat. Biomed. Eng.* **1**, 0077 (2017).

44. G. R. Doak, K. L. Schwertfeger, D. K. Wood, Distant relations: Macrophage functions in the metastatic niche. *Trends Cancer* **4**, 445–459 (2018).

45. S. Hiratsuka, A. Watanabe, Y. Sakurai, S. Akashi-Takamura, S. Ishibashi, K. Miyake, M. Shibuya, S. Akira, H. Aburatani, Y. Maru, The S100A8-serum amyloid A3-TLR4 paracrine cascade establishes a pre-metastatic phase. *Nat. Cell Biol.* **10**, 1349–1355 (2008).

46. D. Kaloni, S. T. Diepstraten, A. Strasser, G. L. Kelly, BCL-2 protein family: Attractive targets for cancer therapy. *Apoptosis* **28**, 20–38 (2023).

47. T. Jiang, L. Chen, Y. Huang, J. Wang, M. Xu, S. Zhou, X. Gu, Y. Chen, K. Liang, Y. Pei, Q. Song, S. Liu, F. Ma, H. Lu, X. Gao, J. Chen, Metformin and docosahexaenoic acid hybrid micelles for premetastatic niche modulation and tumor metastasis suppression. *Nano Lett.* **19**, 3548–3562 (2019).

48. S. Hiratsuka, S. Ishibashi, T. Tomita, A. Watanabe, S. Akashi-Takamura, M. Murakami, H. Kijima, K. Miyake, H. Aburatani, Y. Maru, Primary tumours modulate innate immune signalling to create pre-metastatic vascular hyperpermeability foci. *Nat. Commun.* **4**, 1853 (2013).

49. S. Hiratsuka, A. Watanabe, H. Aburatani, Y. Maru, Tumour-mediated upregulation of chemoattractants and recruitment of myeloid cells predetermines lung metastasis. *Nat. Cell Biol.* **8**, 1369–1375 (2006).

50. W. Zhang, S. Song, H. Wang, Q. Wang, D. Li, S. Zheng, Z. Xu, H. Zhang, J. Wang, J. Sun, In vivo irreversible albumin-binding near-infrared dye conjugate as a naked-eye and fluorescence dual-mode imaging agent for lymph node tumor metastasis diagnosis. *Biomaterials* **217**, 119279 (2019).

51. Y. Wu, J. Chen, L. Sun, F. Zeng, S. Wu, A nanoprobe for diagnosing and mapping lymphatic metastasis of tumor using 3D multispectral optoacoustic tomography owing to aggregation/deaggregation induced spectral change. *Adv. Funct. Mater.* **29**, 1807960 (2019).

52. X. Zhu, H. Xiong, Q. Zhou, Z. Zhao, Y. Zhang, Y. Li, S. Wang, S. Shi, A pH-activatable $MnCO_3$ nanoparticle for improved magnetic resonance imaging of tumor malignancy and metastasis. *ACS Appl. Mater. Interfaces* **13**, 18462–18471 (2021).

53. X. Huang, F. Zhang, S. Lee, M. Swierczewska, D. O. Kiesewetter, L. Lang, G. Zhang, L. Zhu, H. Gao, H. S. Choi, G. Niu, X. Chen, Long-term multimodal imaging of tumor draining sentinel lymph nodes using mesoporous silica-based nanoprobes. *Biomaterials* **33**, 4370–4378 (2012).

54. J. Yang, Y. Zhang, X. Wu, W. Dai, D. Chen, J. Shi, B. Tong, Q. Peng, H. Xie, Z. Cai, Y. Dong, X. Zhang, Rational design of pyrrole derivatives with aggregation-induced phosphorescence characteristics for time-resolved and two-photon luminescence imaging. *Nat. Commun.* **12**, 4883 (2021).

55. T. Zhang, H. Gao, A. Lv, Z. Wang, Y. Gong, D. Ding, H. Ma, Y. Zhang, W. Z. Yuan, Hydrogen bonding boosted the persistent room temperature phosphorescence of pure organic compounds for multiple applications. *J. Mater. Chem. C* **7**, 9095–9101 (2019).

56. J. Yang, H. Gao, Y. Wang, Y. Yu, Y. Gong, M. Fang, D. Ding, W. Hu, B. Z. Tang, Z. Li, The odd–even effect of alkyl chain in organic room temperature phosphorescence luminogens and the corresponding in vivo imaging. *Mater. Chem. Front.* **3**, 1391–1397 (2019).

57. Q. Liao, Q. Gao, J. Wang, Y. Gong, Q. Peng, Y. Tian, Y. Fan, H. Guo, D. Ding, Q. Li, Z. Li, 9,9-Dimethylxanthene derivatives with room-temperature phosphorescence: Substituent effects and emissive properties. *Angew. Chem. Int. Edit.* **59**, 9946–9951 (2020).

58. Z. He, H. Gao, S. Zhang, S. Zheng, Y. Wang, Z. Zhao, D. Ding, B. Yang, Y. Zhang, W. Z. Yuan, Achieving persistent, efficient, and robust room-temperature phosphorescence from pure organics for versatile applications. *Adv. Mater.* **31**, 1807222 (2019).